

Channel Characterization and Realization of Mobile Optical Wireless Communications

Zi-Yang Wu[✉], Muhammad Ismail[✉], Senior Member, IEEE, Justin Kong[✉], Member, IEEE,
Erchin Serpedin[✉], Fellow, IEEE, and Jiao Wang[✉]

Abstract—Link instability induced by users’ mobility is one of the challenges of optical wireless communications (OWC) inherited from the propagation nature of light. Hence, good understanding of the optical channel characteristics in dynamic environments plays a vital role in developing robust resource management strategies in OWC networks. Unfortunately, it is quite difficult to collect accurate indoor optical channel data in dynamic environments. In addition, indoor trajectory dataset is not publicly available. To overcome such limitations, this paper proposes a mobile terminal-centric analytical framework that captures the propagation channel characteristics in a mobile OWC network whose downlink is based on visible light and uplink is based on infrared light. We abstract the nature of human behavior by integrating both macro and micro mobility patterns. These patterns are then used to realize the spatio-temporal characteristics of optical wireless channels under long-term environment-confined mobility. The statistics derived from the developed framework indicate that the mobile line-of-sight (LOS) channel gain follows space-time-dependent multiple-peak Nakagami distributions, whereas the non-line-of-sight (NLOS) channel gain adheres to various space-time-dependent single peak distributions under different indoor layouts. The overall distribution of NLOS bandwidth follows space-time-dependent multiple-peak log-logistic distributions in downlinks and space-time-dependent generalized log-logistic distributions in uplinks. Our investigation demonstrates that the indoor layout and the user’s environment-confined mobility pattern significantly impact the LOS dynamics but present limited impact on NLOS components. Motivated by the need for better channel models for mobile OWC, the proposed framework fills up an important gap in literature and help the research community to understand better the indoor optical wireless channel characteristics.

Manuscript received October 1, 2019; revised March 4, 2020 and May 17, 2020; accepted July 7, 2020. Date of publication July 14, 2020; date of current version October 16, 2020. This research was supported in part by the scholarship from China Scholarship Council (CSC) under the Grant 201806080039 and National Natural Science Foundation of China under grant 61836011. Dr. Erchin Serpedin was in part supported by RRSRG 2020 grant. The associate editor coordinating the review of this article and approving it for publication was H. Elgala. (*Corresponding author: Zi-Yang Wu*)

Zi-Yang Wu is with the College of Information Science and Engineering, Northeastern University, Shenyang 110819, China, and also with the Department of Electrical and Computer Engineering, Texas A&M University, College Station, TX 77843 USA (e-mail: ziyangwu@stmail.neu.edu.cn).

Muhammad Ismail is with the Department of Computer Science, Tennessee Tech University, Cookeville, TN 38505 USA (e-mail: mismail@tnstate.edu).

Justin Kong is with the U.S. Army Research Laboratory, Adelphi, MD 20783 USA (e-mail: justin.hb.kong@gmail.com).

Erchin Serpedin is with the Department of Electrical and Computer Engineering, Texas A&M University, College Station, TX 77843 USA (e-mail: eserpedin@tamu.edu).

Jiao Wang is with the College of Information Science and Engineering, Northeastern University, Shenyang 110819, China (e-mail: wangjiao@ise.neu.edu.cn).

Color versions of one or more of the figures in this article are available online at <http://ieeexplore.ieee.org>.

Digital Object Identifier 10.1109/TCOMM.2020.3009256

Index Terms—Optical wireless communications (OWC), visible light communications (VLC), indoor mobile channel model.

I. INTRODUCTION

OPTICAL wireless networks have posed themselves as very promising candidates to support high speed communications, given the scarcity of the radio frequency (RF) spectrum [1]. In this context, several proposals have been made to implement and commercialize visible light communication (VLC) networks, which are also referred to as Light-Fidelity (Li-Fi) networks [2]. Due to constraints related to the mobile terminal (MT) orientation and power, such networks can support VLC in the downlink and infrared (IR) communications in the uplink.

In order to carry out proper management of the network resources, good understanding of the channel characteristics is required. Due to the propagation nature of light, the optical channel is susceptible to burst occlusion and displacement [3]. Therefore, the details of the environment and MT-centric trajectory based on the combination of user trajectory and terminal orientation dominate the variations in the channel states. It should be highlighted that the wavelength of light is only a few hundred nanometers, and thus, it is almost impossible for light to bypass the macro obstacles by diffraction. This results in frequent outages in line-of-sight (LOS) transmissions when the user is moving in a complex indoor environment. Hence, the specific motion trajectory determines the quality of the LOS transmission. In other words, the observed pattern of the LOS channel is a projection of the environment-confined mobility pattern.

Unfortunately, our mastery of indoor mobility patterns is very limited. One of the reasons is that the source of mobility, i.e., accurate indoor motion trajectory data, is not readily available [4]. Another factor is the lack of high-quality channel data sets. From the perspective of practical measurements, if participants use smart terminals to collect a sizable dataset, it is hard to achieve enough accuracy of optical intensity measures in order to capture meaningful statistics under mobility. In this paper, we aim to establish a framework that is capable of producing trajectories in indoor scenarios, with which mobile optical channels can be properly characterized.

A. Related Work

Mobility support in optical channels involves understanding the patterns of the terminal’s mobility as well as the propagation features of light.

1) Channel Models: The first step in modeling an optical channel is to study the radiation pattern of a light source. Moreno and Sun [5] proposed a general and accurate representation for the radiation pattern of a light-emitting diode (LED). The pattern was expressed as the sum of two or three Gaussian or cosine-power functions. However, in a lighting-supported environment, LEDs are usually grouped as arrays rather than as single point sources. Ding *et al.* [6] compared the channel characteristics of both the simplified point-source model and several practical cases using various scales of arrays. As for the generation of the channel impulse response (CIR), Kahn and Barry [7] summarized the modeling and simulation methods of ray tracing for wireless infrared communications. Schulze [8] presented a frequency-domain simulation method for an infinite number of reflections. More detailed channel models for VLC were given by Lee *et al.* [9] and were further developed by Jungnickel *et al.* [10]. The ray tracing methods for VLC were introduced by Rodríguez *et al.* [11] and for efficient non-line-of-sight (NLOS) channel computation by Chen *et al.* [12]. The aforementioned efforts provide a solid foundation for static channel models and analysis. On the other hand, limited research works considered mobile scenarios. For instance, the mobile channel model proposed by Miramirkhani *et al.* [13] exhibits significant variations in the received power along a straight line trajectory; also, Chvojka *et al.* [14] presented analytical and experimental results to model the impact of random movements in various indoor scenarios, where both shadowing and blocking effects were investigated. More recently, Soltani *et al.* [15] proposed an orientation-based random waypoint (ORWP) mobility model. However, existing channel models in a dynamic environment usually assume over-simplified mobility models which cannot reproduce a realistic and comprehensive human trajectory (e.g., [13]–[15]).

2) Mobility Models: Although random walk models such as random waypoint used in e.g. [15]–[18] are popular and straightforward, they fail to reflect human mobility accurately from the perspective of the nature of human movement instincts and the features of dynamic MT orientation. On the other hand, bounded Lévy-walk with heavy-tail distance and pause-time distributions is statistically more suitable to model human mobility [19]. Different from the behaviors in conventional random walk models, real human trajectories exhibit strong tendency to return to the visited locations and manifest through recurrence and temporal periodicity in human mobility [20]. From this perspective, the human trajectory is predictable. Besides, more importantly, the vital statistical characteristics of individual trajectories are largely indistinguishable regardless of their spatio-temporal scales [20]. All statistic results collectively confirm that human mobility is characterized by scale-freedom in which, however scales, human trajectories exhibit similar patterns to those of a Lévy-walk [19]. Therefore, the same statistical characteristics of Lévy-walk and return tendency can be both deployed in indoor environments after reducing the scale.

Unfortunately, existing mobility models do not capture macro and micro patterns that best reflect human behavior in an indoor scenario. In this context, while Lévy-walk and return tendency-based models can be used

to describe the next destination point for a mobile user (i.e., macro pattern), the detailed trajectory between the origin and destination (i.e., micro patterns) that accounts for path selection [21], steering forces [22] and orientation of MTs [15], [23]–[25] should be captured.

B. Contributions

In order to address the limitations of the existing models and hence offer an accurate tool for proper characterization and realization of optical wireless channels, we have carried out the following contributions herein paper:

- We propose a mobility model that better captures the nature of human mobility. A macro pattern featured by a semi-Markov renewal process subject to Lévy-walk and return regularity, and a micro pattern featured by the shortest path, steering behavior, and random MT orientations are introduced and integrated all together within the proposed model.
- We establish a systematic framework that allows to generate mobile trajectories based on the proposed mobility model, which is then used to generate CIR dataset. Key parameters of this framework are obtained from fitting measurement statistics in real-world from anonymous mobility collections.
- We use the developed framework to characterize the channel of indoor mobile optical wireless networks with VLC support in the downlink and infrared communications support in the uplink, at a practical time and space scale, where blockages from furniture and user body are considered.
- The statistical properties of mobile optical wireless channels are analyzed from both time and space perspectives. We conclude a space-time-dependent statistical patterns on channel gain, bandwidth and outage probability, which dramatically evolve over the environment-confined mobility.

The rest of this paper is organized as follows. Section II presents the proposed indoor mobility model that captures both macro and micro realistic mobility patterns. Section III discusses the proposed framework to generate the CIR data in a dynamic environment using the proposed mobility model. Section IV interprets how to collect key mobility parameters from the real-world and gives the system parameter setup to generate the dataset. Section V presents a set of results to characterize the optical wireless channel for both LOS and NLOS links. Conclusions are drawn in Section V.

II. MOBILITY MODEL

Fig. 1 shows the hierarchy of the proposed framework in this paper. As shown in Fig. 1, we start by introducing a realistic mobility model that captures the human behavior on different spatio-temporal scales, namely:

- *Macro patterns:* These define the next destination points and are modeled as a semi-Markov renewal process subject to bounded Lévy-walk and return regularity.
- *Micro patterns:* These define the detailed trajectory between the origin and destination points along with the MT orientation and are represented by a large-scale

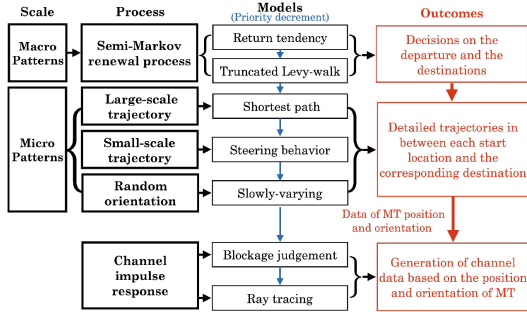


Fig. 1. Hierarchy of the proposed framework to generate CIR in dynamic optical wireless channels.

trajectory subject to the shortest path, a small-scale trajectory featuring steering behavior, and a random terminal orientation.

A. Macro Patterns

The macro-scale mobility patterns are described using a semi-Markov renewal process [26]. Through statistical analysis [26], the return regularity and truncated Lévy-walk dominate the transition probabilities among different destination points (states) in this process.

The destination set is defined consistently with various types of furniture and entrances within a room. Each type of furniture has a particular mean sojourn time, which defines the time a user dwells in the range of the furniture. At this level, it is assumed that the semi-Markov renewal process is time-homogeneous and represented by $\{(X_n, T_n) : n \geq 0\}$ with discrete state space of residential destinations $\mathcal{L} = \{1, 2, 3, \dots, L\}$ (the furniture and entrances) where T_n is the time of the n th transition, X_n is the state at the n th transition [26], and L stands for the number of the destinations including all the resident nodes and entrances. The state of a semi-Markov process represents each destination, and traveling from one destination to another is a state transition.

The choice of each destination is first determined by return regularity, by which the user decides to return to a particular destination. It is important to note that return regularity is different from the general random walk model. In contrast with the smooth asymptotic behavior predicted for random walks [20], in realistic human trajectories, there always exists a recurrence and temporal periodicity inherent to human mobility as returning to a specific place with a strong tendency to locations they visited before in a particular time. For the sake of characterizing this return tendency, the semi-Markov process should cover the stage-of-trajectory T_d (e.g., morning, noon, afternoon, and night) during each transition [27]. Accordingly, we consider the time-homogeneous semi-Markov kernel, which denotes the probability of transition into state $j \in \mathcal{L}$ within t units of time immediately after the transition into state $i \in \mathcal{L}$ as

$$\begin{aligned} & \zeta_{i,j}^{(T_d)}(t) \\ &= p_{i,j}^{(T_d)} \mu_{i,j}^{(T_d)}(t) \\ &= \Pr\{X_{n+1} = j, T_{n+1} - T_n \leq t | X_n = i, T_{n+1}, T_n \in T_d\}, \end{aligned} \quad (1)$$

where $p_{i,j}^{(T_d)}$ is the transition probability from start location i to destination j defined as $p_{i,j}^{(T_d)} = \lim_{t \rightarrow \|T_d\|_\infty} \zeta_{i,j}^{(T_d)}(t) = \Pr\{X_{n+1} = j | X_n = i, T_{n+1}, T_n \in T_d\}$. In (1), $\mu_{i,j}^{(T_d)}$ denotes the time distribution including: a) the duration of dwelling at state i , t_s and b) the transition into the destination j , $t_{i \rightarrow j}$. We have $\mu_{i,j}^{(T_d)}(t) = \Pr\{T_{n+1} - T_n \leq t | X_{n+1} = j, X_n = i, T_{n+1}, T_n \in T_d\}$.

In the general movement during the absence of the return action, the bounded Lévy-walk plays the decisive role in each transition. The truncated Pareto distribution characterizes this pattern. All statistic results collectively confirm the scale-freedom characterization of human mobility [19], [20]. Human movements share similar patterns on any scale since the key statistical characteristics of re-scaled individual trajectories are identical. Hence, even for the indoor trajectories, this truncated heavy-tail distribution contributes prominently. Lévy-walk is a kind of continuous-time random walk. We consider a random walker and choose the joint space-time probability density function (PDF):

$$\Phi(r_{i \rightarrow j}, t_{i \rightarrow j}) = \phi(t_{i \rightarrow j} | r_{i \rightarrow j}) p(r_{i \rightarrow j}), \quad (2)$$

where $p(r_{i \rightarrow j})$ is the probability that a step of length $r_{i \rightarrow j}$ occurs and $\phi(t_{i \rightarrow j} | r_{i \rightarrow j})$ is the conditional probability density that such step takes $t_{i \rightarrow j}$ time in movement. When $p(r_{i \rightarrow j})$ is a heavy-tailed distribution such as Pareto distribution, the mobility specified by $\phi(t_{i \rightarrow j} | r_{i \rightarrow j})$ is a Lévy-walk. Unifying this definition with our previous discussion on semi-Markov process, we assign the destination j with respect to the start i with its Euclidean metric $r_{i \rightarrow j}$ via the PDF of a truncated Pareto distribution as

$$p_{i,j} = p(r_{i \rightarrow j}) = \frac{\alpha(r_{\min})^\alpha r_{i \rightarrow j}^{-(\alpha+1)}}{1 - (r_{\min}/r_{\max})^\alpha}, \quad (3)$$

in which α is a positive parameter, $r_{\min} = \min_{\forall a,b \in \mathcal{L}} \{r_{a \rightarrow b}\}$ and $r_{\max} = \max_{\forall a,b \in \mathcal{L}} \{r_{a \rightarrow b}\}$. Also, the sojourn time t_s that a user dwells in a residential location i is also subjected to a truncated Pareto distribution [19] as $p_{t_s}(t_s; \beta, t_{s,\max}^{(i)}, t_{s,\min}^{(i)}) = \beta(t_{s,\min}^{(i)})^\beta t_s^{-(\beta+1)} / \left(1 - (t_{s,\min}^{(i)}/t_{s,\max}^{(i)})^\beta\right)$, where β corresponds to the positive parameter, $t_{s,\max}$ and $t_{s,\min}$ are the maximum and minimum sojourn times at the current location, respectively.

However, the corresponding time steps $t_{i \rightarrow j}$ in $\phi(t_{i \rightarrow j} | r_{i \rightarrow j})$ is determined by a two-scale trajectory model regarding the transition $i \rightarrow j$, which will be interpreted in the following subsection. All the statistical results we are referring to base on the data collection using the distance between any two resident spots rather than actual trajectory length in detail. Therefore, to stick with the status quo, the step distance in (3) is not the exact length in a real trace, but the straight line distance.

B. Micro Patterns

The micro pattern details the trajectories between every start to its destination as $\Theta(i, j, t)$, based on a two-level model: large-scale and small-scale descriptions. The large-scale one

describes the movement path where the user follows a sequence of intermediate target nodes; while the small-scale one includes the 3D successive user positions and orientations.

In this paper, we only focus on mobile states, where the link quality is under serious challenge due to mobility. As aforementioned, the action of choosing a destination is dominated by the bounded Lévy-walk process and return tendency in the macro pattern, so in this subsection, large-scale mobility is defined by the shortest path according to the Dijkstra algorithm [21]. The graph of resident nodes (destinations) \mathcal{G}_r for furniture and path nodes (grid) \mathcal{G}_p for the endpoints of segments in the path are deployed. \mathcal{G}_p represents all the possible transitions between furniture and is arranged for the clearance of the impassable area. Meanwhile, \mathcal{G}_p has all the resident nodes for covering the starts and ends of every trace. The extra nodes associated with the doors for engaging the entering and exiting mobility as $\mathcal{G}_r \subset \mathcal{G}_p$. These graphs ought to keep the user from the unreal trajectory. \mathcal{G}_r allows the user to choose an item of furniture as a destination following the macro pattern, and \mathcal{G}_p ensures a path to each destination. A feasible path $\mathcal{V}_{i \rightarrow j}$ from the resident location i to the location j is yielded using the Dijkstra shortest path algorithm \mathcal{D} :

$$\mathcal{V}_{i \rightarrow j} = \mathcal{D}(i, j), \quad (4)$$

which is a sequence of successive path nodes.

In addition to the given path $\mathcal{V}_{i \rightarrow j}$, when encountering the departure, human mobility in a smaller scale that encodes the detailed trajectories is described by steering behavior model presented in [22]. Steering behavior \mathcal{S} is brought to bear on the interactions between the user and environment Ω so that one can reproduce a simple physical engine upon the path node sequence as

$$\Theta(i, j, t) = \mathcal{S}(\mathcal{V}_{i \rightarrow j}, \Omega). \quad (5)$$

Typically, the user is treated as a point particle that carries a point mass m , maximum acceleration a_{max} and a maximum velocity of v_{max} . Then, the very basic Newton's laws of motion can be applied, where the user is driven by several steering forces applied on their center of mass. At time step t , the acceleration $a(t)$ is renewed according to the resulting steering force applied on the user. The applied acceleration vector $\mathbf{a}(t)$ is given by $\mathbf{a}(t) = \mathbf{F}(t)/m$. The resulting velocity $\mathbf{v}(t)$ is approximated by the Euler integration as an augment of the product of the current acceleration vector with the time interval δ_τ to the previous velocity, i.e., $\mathbf{v}(t) = \mathbf{v}(t - \delta_\tau) + \mathbf{a}(t) \delta_\tau$. The position $\mathbf{p}(t)$ is obtained by the Euler integration as an augment of the product of the current applied velocity vector with the time interval δ_τ upon the previous position, i.e., $\mathbf{p}(t) = \mathbf{p}(t - \delta_\tau) + \mathbf{v}(t) \delta_\tau$. On this basis, it is necessary to formulate the details of the steering forces to illustrate how the human-like behaviors might unfold. In this paper, for the sake of simplicity, a single user is assumed, and thus only seek and avoidance behaviors are considered.

The seek behavior produces a seek force for attracting the user to each target node in the successive node sequence along the selected path. The seek force orients towards the distance vector $\mathbf{d}(t)$ between the intermediate target $\xi(t) \in \mathcal{V}_p$ and the

actual position of the user $\mathbf{p}(t)$ as $\mathbf{d}(t) = \xi(t) - \mathbf{p}(t)$. Hence, the corresponding desired velocity vector $\mathbf{v}^d(t)$ is given by $\mathbf{v}^d(t) = \frac{\mathbf{d}(t)}{\|\mathbf{d}(t)\|} \frac{v_{max}}{\delta_\tau}$, where $\|\cdot\|$ represents the 2-norm of vector. Following the velocity difference between the actual velocity and the desired velocity, the user is driven by the seeking force $\mathbf{F}_s(t)$ as $\mathbf{F}_s(t) = m \frac{\mathbf{v}^d(t) - \mathbf{v}(t)}{\delta_\tau}$. Contrary to seeking, while approaching the destination, the user also slows down to end the period of mobility. This behavior is modeled by arrival force $\mathbf{F}_a(t)$ that is a reverse to $\mathbf{F}_s(t)$ but with a threshold radius to ignore long range effects.

On the other hand, to repulse a user from penetrating insurmountable areas such as the layout of furnishings, an avoidance force ought to be applied upon the user. Considering the perpendicular distance from the present position to one of the surfaces of obstacles, the avoidance force $\mathbf{F}_o(t)$ is given by $\mathbf{F}_o(t) = m \frac{\hat{\mathbf{n}} \frac{\|\mathbf{v}(t) - \mathbf{v}(t - \delta_\tau)\|}{d_w(t)}}{\delta_\tau}$, in which d_w is the perpendicular distance to blockage surface w , and $\hat{\mathbf{n}}$ denotes an orthogonal unit vector against w .

By taking all behaviors into account, we express the resulting force as

$$\mathbf{F}(t) = \mathbf{F}_s(t) + \gamma_o \sum_w \mathbf{F}_o(t) + \gamma_a \mathbf{F}_a(t), \quad (6)$$

where γ_o is the ratio of avoidance force to seek force, and γ_a stands for the ratio of arrival force to seek force, and W indicates the number of surfaces of all blockages with an effective distance threshold for the sake of neglecting the remote surfaces so as to improve the computational efficiency. Finally, we will have to limit the scale of the force: $\mathbf{F}(t) := \max \{ \|\mathbf{F}(t)\|, ma_{max} \} \frac{\mathbf{F}(t)}{\|\mathbf{F}(t)\|}$.

The micro pattern of mobility also models the random orientation of the mobile terminal [15]. The indoor optical wireless channel can be treated as a slowly-varying channel since its delay spread is typically on the order of nanoseconds, and the coherence time of the random orientation is in the order of hundreds of milliseconds [15], [28]. Rotation geometry for user equipment usually requires three elemental angles called yaw, pitch, and roll. The concatenated rotation matrix with respect to the Earth coordinate system indicates the rotated normalized vector represented in the spherical coordinate system with the polar angle ϑ and azimuth angle ω . The polar angle is between the rotated normalized vector and the vector perpendicular to the ground plane; the azimuth angle stands for the projection of the rotated unit vector in the ground plane regarding the positive direction of meridian. The statistics from real-world [15], [28] show that the polar angle should be modeled as a Laplace distribution $\vartheta \sim \text{Laplace}(\mu_s, b_s)$ for the sitting activity and a Gaussian distribution $\vartheta \sim \mathcal{N}(\mu_w, \sigma_w)$ for the walking activity. In this paper, the azimuth angle is obtained directly from user trajectories. Meanwhile key parameters μ_s , b_s , μ_w and σ_w are resolved from measurements in real-world according to the methodology in [15].

III. GENERATION OF MOBILE CHANNEL DATA

We first generate the complete trajectories and mobility data $\mathbf{M}(t)$ following the model described in Section II that integrates the macro and micro patterns. The procedures

Algorithm 1 State Machine for Generating Mobility

```

1: Initialize the room layout, the resident and path nodes
2: Initialize EventList for recording the statuses
3:  $\mathbf{p}(t=0) = \mathbf{p}_{door}$  as the user enters the door
4:  $EventList(t=\delta_\tau) \leftarrow "Sojourn"$ ,
5:  $EventList(t=2\delta_\tau) \leftarrow "Depart"$ ,  $t \leftarrow 2\delta_\tau$ 
6: Set the first destination  $j$  according to  $p(r_{i \rightarrow j} | \mathbf{p}_{door})$ 
7: while  $\|\mathbf{p}(t) - \mathbf{p}_{door}\| > \epsilon$  do
8:    $EventList(t_{return}) \leftarrow "Return"$  according to (1)
9:   switch  $EventList(t)$ 
10:    case "Depart" do
11:       $i \leftarrow \mathbf{p}(t)$ 
12:      Execute micro trace generation and get  $t_{arrival}$ ,  

EventList, and  $\Theta(i, j, t)$ 
13:      Update mobility status  $\mathbf{M}(t) \leftarrow \Theta(i, j, t)$ 
14:    case "Arrive" do
15:      Update mobility status  $\mathbf{M}(t) \leftarrow \Theta(i, j, t)$ 
16:      Generate  $t_s \sim \text{Pareto}(\beta, t_{s,\max}, t_{s,\min})$ 
17:       $t_{departure} \leftarrow t_{arrival} + t_s$ 
18:      Choose destination  $j$  according to  $p(r_{i \rightarrow j} | i)$  as (3)
19:       $EventList(t \sim t_{departure} - \delta_\tau) \leftarrow "Sojourn"$ 
20:       $EventList(t_{departure}) \leftarrow "Depart"$ 
21:    case "Sojourn" do
22:      Update sitting motion status  $\mathbf{M}(t)$ 
23:    case "Return" do
24:      Reset EventList from time slot  $t$ 
25:       $i \leftarrow \mathbf{p}(t)$ ,  $j \leftarrow \mathbf{p}_{Return}$ 
26:      Execute micro trace generation and get  $t_{arrival}$ ,  

EventList, and  $\Theta(i, j, t)$ 
27:      Update mobility status  $\mathbf{M}(t) \leftarrow \Theta(i, j, t)$ 
28:    case "Transit" do
29:      Update mobility status  $\mathbf{M}(t) \leftarrow \Theta(i, j, t)$ 
30:    end switch
31:     $t \leftarrow t + \delta_\tau$ 
32: end while
33: return  $\mathbf{M}$ 

```

of producing macro mobility are given in Algorithm 1, where we organize the mobility into five statuses as follows: (1) "Return": the movements due to the return regularity; (2) "Arrive": the behaviors of choosing the sojourn duration and the next destination; (3) "Sojourn": the implementation of the sojourn behavior at resident nodes; (4) "Depart": the behaviors of choosing the trajectories $\Theta(i, j, t)$; (5) "Transit": the implementation of the chosen trajectories. Also, Algorithm 2 gives the details on producing the micro mobility in the trajectories of $\Theta(i, j, t)$.

In this paper, we consider the blockage of opaque objects from furniture and user body before calculating the specific channel gain of each link. Standard procedures with judging the viability of each ray in advance are demonstrated as follow. In the aforementioned coordinate system, the receiver incidence angle θ is decided by ϑ and ω and the relative angle between a transmitter and a receiver according to the configuration of the placement of the transceiver on the terminal. Also, because we need to reduce the potential harm of the irradiation to the eyes from uplink and the probability of the blockages from the user body that will induce considerable outages, the transceiver on an MT should point forward the trace direction rather than towards the ceiling perpendicular to the surface of screen in the mobility. Therefore, we define a direction vector for a terminal transceiver as

Algorithm 2 Generation of Micro Trajectory: $\Theta(i, j, t)$

```

1:  $\mathbf{p}(t) \leftarrow i$ ,  $t_i = t$ 
2: Get adjacent matrix for  $i, j$  from  $\mathcal{G}_p$ 
3: Deploy Dijkstra algorithm:  $\mathcal{V}_{i \rightarrow j} = \mathcal{D}(i, j)$ 
4: Set a margin  $\epsilon$  for checking if the user arrives the range of  

a node.
5: while  $\|\xi(t) - j\| > \epsilon$  do
6:   if  $\xi(t) = j$  then
7:     if  $\|\mathbf{p}(t) - \xi(t)\| < \epsilon$  then
8:       goto ending
9:     else
10:       $\mathbf{F} \leftarrow \mathbf{F}_s(t) + \gamma_o \sum_w^W \mathbf{F}_o(\mathbf{d}_w(t), t) + \gamma_a \mathbf{F}_a(t)$ 
11:    end if
12:  else
13:    if  $\|\mathbf{p}(t) - \xi(t)\| < \epsilon$  then
14:       $\xi(t) \leftarrow \xi(t + \delta_\tau) \in \mathcal{V}_{i \rightarrow j}$ 
15:    else
16:       $\mathbf{F}(t) \leftarrow \mathbf{F}_s(t) + \gamma_o \sum_w^W \mathbf{F}_o(\mathbf{d}_w(t), t)$ 
17:    end if
18:  end if
19:  Generate  $\vartheta(t) \sim \mathcal{N}(\mu_w, \sigma_w)$ 
20:  Get  $\mathbf{v}(t)$  and  $\mathbf{p}(t)$ 
21:   $\Theta(i, j, t) \leftarrow (\mathbf{v}(t) | \mathbf{p}(t) | \vartheta(t))$ 
22:   $t \leftarrow t + \delta_\tau$ 
23: end while
24: ending:
25:  $t_{arrival} \leftarrow t$ 
26:  $EventList(t_i \text{ to } t_{arrival} - \delta_\tau) \leftarrow "Transit"$ 
27:  $EventList(t_{arrival}) \leftarrow "Arrive"$ 
28: return  $\Theta(i, j, t)$  and EventList

```

$\mathbf{u}_\theta^{UL}(t) = (\sin \vartheta(t) \cos \omega(t), \sin \vartheta(t) \sin \omega(t), \cos \vartheta(t))$, and for a base station (BS) transceiver as $\mathbf{u}_\theta^{DL} = (0, 0, -1)$. Then, we get $\cos \theta(t) = \mathbf{u}_\theta^{UL}(t) \cdot \mathbf{u}_\theta^{DL} / (\|\mathbf{u}_\theta^{UL}(t)\| \cdot \|\mathbf{u}_\theta^{DL}\|)$. Additionally, we get the transmission distance of LOS as $d_0(t) = \|\mathbf{p}(t) - \mathbf{p}_{BS(v)}\|$, where $\mathbf{p}_{BS(v)}$ corresponds to the location of the BS $v \in \{1, \dots, v, \dots, V\}$ in which V is the number of BSs. Hence, before the computation on the channel gain for a single ray, if any intersection between this ray with any of the surfaces including the furniture and the user body is found, we judge this ray as blocked.

Given a cubic environment Ω that occupies a certain volume, the overall time-varying impulse response h_Ω is defined as

$$h_\Omega(t, \tau) = \sum_{k=0}^{\infty} h^{(k)}(t, \tau), \quad (7)$$

where k denotes the index of reflections and τ represents the delay. The total channel gain is defined as the direct-current (DC) gain $H(t, 0) = \int_{-\infty}^{\infty} h_\Omega(t, \tau) d\tau$. The LOS impulse response is given by

$$h^{(0)}(t, \tau) = \begin{cases} \frac{A_R}{d_0^2(t)} \frac{(m+1)}{2\pi} \cos^m \psi(t) \cos \theta(t) \\ \times T_S(\theta(t)) \delta\left(\tau - \frac{d_0(t)}{c}\right), \\ \text{if } 0 \leq \theta(t) \leq \Psi \\ 0, \text{ if } \theta(t) > \Psi \text{ or ray is blocked,} \end{cases} \quad (8)$$

where A_R is the sensor area, ψ stands for the angle of irradiance, Ψ is the receiver's field-of-view (FOV), c means the speed of light, and $T_S(\theta)$ denotes the overall transmission

response of the optical system and is treated as 1 in this paper. Besides, the mode number m is related to half power angle $\Phi_{1/2}$ via $m = -\ln 2/\ln \cos \Phi_{1/2}$. For the diffused NLOS links, a recursive ray-tracing method [29] is adopted and microelements $\{\varepsilon\}$ representing differential of reflective areas are considered. For path $k > 1$, the intermediate propagation from a small cell ε_n to another one ε_m contributes to the NLOS response recursively as

$$h^{(k)}(t, \tau) = \sum_{m=1}^M \sum_{n=1}^N h_{\varepsilon_m \rightarrow \varepsilon_n}^{(k-1)}(t, \tau) * \rho_\varepsilon h_{\varepsilon_n \rightarrow R}^{(0)}(t, \tau), \quad (9)$$

in which R denotes the receiver, ρ_ε is the reflectivity of the surface to which the element belongs. In addition, we divide the reflective surfaces into N elements with the FOV as 90° [9], [14]; especially for $k = 1$ and transmitter S , we have propagation $S \rightarrow \varepsilon$ instead of the ones among other elements expressed as

$$h^{(1)}(t, \tau) = \sum_{n=1}^N h_{S \rightarrow \varepsilon_n}^{(0)}(t, \tau) * \rho_\varepsilon h_{\varepsilon_n \rightarrow R}^{(0)}(t, \tau), \quad (10)$$

where

$$h_{S \rightarrow \varepsilon}^{(0)}(t, \tau) = \begin{cases} \frac{A_\varepsilon}{d_{S, \varepsilon}^2(t)} \frac{(m+1)}{2\pi} \cos^m \psi_{S, \varepsilon}(t) \cos \theta_{S, \varepsilon}(t) \\ \times \delta\left(\tau - \frac{d_{S, \varepsilon}(t)}{c}\right), \\ \text{if } 0 \leq \theta_{S, \varepsilon}(t) \leq 90^\circ \\ 0, \text{ if } \theta_{S, \varepsilon}(t) \geq 90^\circ \text{ or ray is blocked.} \end{cases} \quad (11)$$

$$h_{\varepsilon \rightarrow R}^{(0)}(t, \tau) = \begin{cases} \frac{A_R}{d_{\varepsilon, R}^2(t)} \frac{(m+1)}{2\pi} \cos^m \psi_{\varepsilon, R}(t) \cos \theta_{\varepsilon, R}(t) \\ \times T_S(\theta_{\varepsilon, R}(t)) \\ \text{if } 0 \leq \theta_{\varepsilon, R}(t) \leq 90^\circ \\ 0, \text{ if } \theta_{\varepsilon, R}(t) \geq 90^\circ \text{ or ray is blocked.} \end{cases} \quad (12)$$

The computational cost of this recursive approach is $(N)^K$, where K is reflection number, and N is the number of elements into which the reflecting surfaces are divided. Meanwhile, the Monte-Carlo ray-tracing algorithm can be more efficient as the computational cost can be $K \cdot N_{Ray} \cdot N_F$, where N_{Ray} stands for the number of rays which is set for accuracy, and N_F corresponds to the number of triangles for defining the geometry. However, in this work, we rely on a huge amount of dataset to capture the spatio-temporal evolution of the channel statistics in a macro aspect, therefore, we consider $K = 1$ as the contribution of the higher order reflections ($K \geq 2$) is very small compared to that of the LOS and $K = 1$ components as demonstrated in [30]. As such, the computational cost difference between these two methods is very small, and eventually we choose the deterministic one with more accurate outcomes.

IV. SYSTEM SETUP

A. Measurement Setup

Rather than setting the mobility parameters arbitrarily, we had set a rich body of experiments and measurements

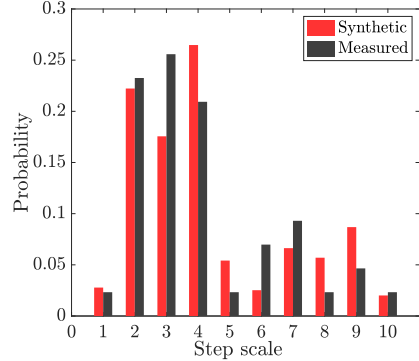


Fig. 2. Statistical analysis of indoor trajectories. All the steps are categorized into several step scale levels. The step scale distribution of our proposed synthetic trajectory is compared with the measurement results from real-world in a similar office room, where $\alpha = 0.5$ for choosing the destination distances.

on real-world indoor mobility through volunteers' daily lives using cell phones to collect traces, so that we can decide the parameters that approximate real mobility as much as possible. However, due to lacking high-resolution detection of light intensity and indoor position using commercial smart phones, in this paper, we collected the records on terminal orientation and visited locations via an application named "phyphox" [31] from 20 participants who came from different types of offices and laboratories without violating their privacy. These data cannot directly be used in further channel modeling, but they are analyzed to determine the critical parameters in the proposed mobility framework. Please note that "phyphox" is used for collecting the records on terminal orientation and visited spot but not the detailed trajectories since GPS does not have a good accuracy for indoor scenarios. Sometimes its error might exceed 10 m. In this work, we restricted several types of offices and laboratories with known layouts. Therefore we can quantify the accurate location of a visited spot such as a bookshelf based on an approximate location record when the participant dwells there. We measure the distance between each two nodes in a room and categorize the distances into 10 step scale levels for a room. Accordingly, we can get the dimensionless statistics generalized for any indoor layout in any size. The step scale in Fig. 2 is therefore obtained by categorizing the distance between two successive identified visited spots. This is why the indoor mobility is still a vital challenge in mobile OWC: we cannot get accurate indoor trajectories dataset, and thus we cannot carry out further data-driven investigation accurately. This is however also our motivation: to generate arbitrarily large-size dataset on indoor OWC by reproducing the mobility based on statistics measured from real-world that represents human behavior nature.

The first key parameter is α in the bounded Lévy-walk model characterized by Pareto distribution. We analyzed the records on visited spots associated with the step lengths, then estimated an approximation of α as 0.5 for choosing destination distances. As shown in Fig. 2, after adopting the same α , we get a very similar pattern on the probability distribution of synthetic step scales compared to 307 complete records of measured traces. Note that since the step size in the room is highly relevant to the layout such as the distances among various furnishings, some step scales cannot be reached

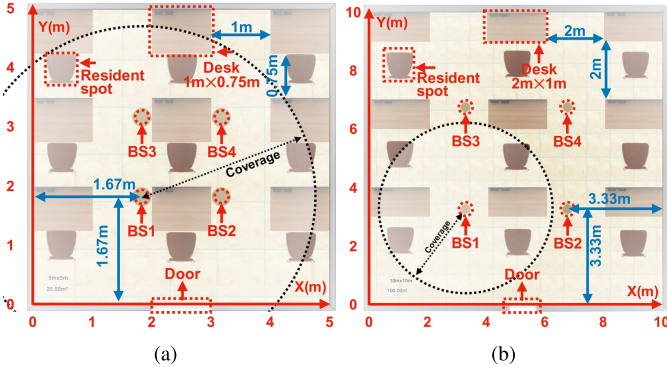


Fig. 3. (a). Room layout of $5\text{m} \times 5\text{m} \times 3\text{m}$ setup. (b). Room layout of $10\text{m} \times 10\text{m} \times 3\text{m}$ setup. Four light BSs are distributed evenly on the ceiling plane.

in a fixed layout. In addition, we determined the parameters for terminal orientations and used the same methodology in [15] and concluded that for sitting motion: $\mu_s = 45.11$ and $\sigma_s = 7.84$, and for walking motion: $\mu_w = 31.79$ and $\sigma_w = 7.61$, which agree with the results in [15]. The difference might be due to the difference in room layout, user behavior, measurement accuracy, and even data amount.

B. Synthetic Setup

In our work, the room layout and all objects are modeled in the form of cuboid. Specifically, the user body is set as a $1.8\text{ m} \times 0.2\text{ m} \times 0.45\text{ m}$ cuboid, where MT is being held at the height of 1.3 m while walking and 1 m while sitting, and at a distance of 0.2 m away from the user's orientation. In the $5\text{ m} \times 5\text{ m} \times 3\text{ m}$ room layout shown in Fig. 3(a), all the desks are set at 1 m length and 0.75 m width with partition height of 1.3 m . In the $10\text{ m} \times 10\text{ m} \times 3\text{ m}$ room layout shown in Fig. 3(b), the desks are set at 2 m length and 1 m width with partition height of 1.3 m . We treat all the surfaces in the environment as reflectors, including user bodies. All the cuboids are considered as 5 reflective and opaque surfaces (the bottom surfaces are ignored). Also, the mass of the user is set as 70 kg with a maximum walking speed of 2.1 m/s , and a maximum acceleration of 1 m/s^2 [32]. The generated mobility sample interval δ_τ is 100 ms . The trajectory duration determined by return regularity follows a Gaussian distribution with a mean of 1000 samples and a standard deviation of 50 . For the sojourn duration at each resident node, we assume $\beta = 1$ and randomly select $t_{s,\max}$ and $t_{s,\min}$ for each furniture. However, our work only reflects movement impacts, which means the detailed model of sojourn behavior is not in the scope of our investigation. All the statistics we derive for the optical channel are deemed during users' mobility without sojourn state since the existing literature has given plenty of results on OWC under stationary state. However, interested readers still could synthesize the complete trajectory data including sojourn state using our framework.

According to the procedures we have introduced in the preceding sections, we produce the human trajectories dataset as demonstrated in Fig. 4(a) and (c). In Fig. 4(b) and (d), we illustrate the spatial distribution of trajectories, in which, the frequency of each unit area being visited is calculated, and we only show the case of moving. Fig. 4(b) and (d)

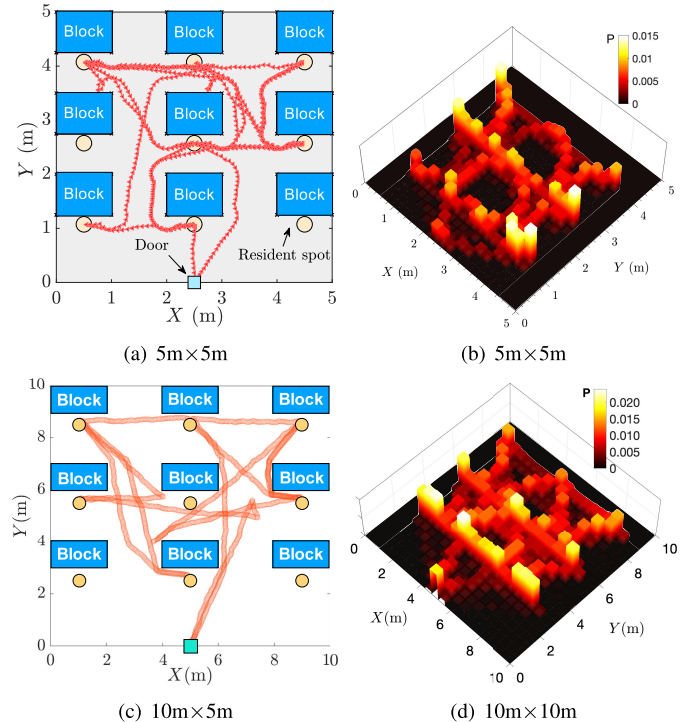


Fig. 4. In (a) and (c), the examples of reproduced trajectory are given. In (b) and (d), the frequency of each unit area being visited is calculated from the generated dataset.

TABLE I
PARAMETERS FOR TRANSCEIVERS

BS number	4
$\Phi_{1/2}$	60°
A_R	100 mm^2
Ψ	45°
VLC wavelength	$380\text{ nm to }780\text{ nm}$
VLC ρ_e	0.7 (walls), 0.2 (other surfaces)
IR wavelength	800nm
IR ρ_e	0.8 (walls), 0.5 (other surfaces)
ε area	10^4 mm^2
{ ε } model	Lambert

demonstrates a higher probability of passing by the resident nodes than the crossing paths, and a higher probability in the resident nodes and path located along the central row than other rows, and a higher probability around turning corners than typical paths.

Table I summarizes the transceiver parameters used following most of the existing lecture [9], [14], [33] while generating the channel datasets. The channel model we present in this paper is applicable to both VLC and IR. However, due to the wideband nature of the VLC link [9], the reflectance of materials in the visible light spectrum should be taken into account. In this work, for simplicity, we assume a certain light-emitting spectral power distribution of transmitters such that the resulting reflectance of VLC and IR can be treated as in Table I. Interested readers can adopt more detailed spectral reflectance of materials based on actual measurements if necessary. When generating the channel information, we set the MT transceivers located at the center of the top of the phone pointing to the azimuth direction. Four light BSs are located evenly on the ceiling as illustrated in Fig. 3(a) and (b)

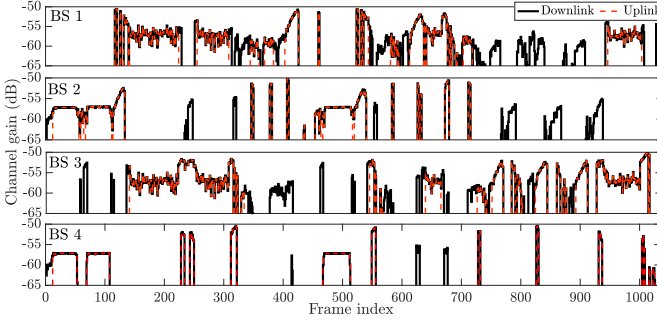


Fig. 5. Illustration of the LOS channel gain linked with 4 light BSs for both uplink and downlink during an entire trajectory, where the sample interval is 100 ms.

for both layouts. The orthogonal bands can be allocated to these BSs. We consider the transmit power of each BS as a dimensionless unit power, because we only focus on the channel gain. The time resolution for CIR is 0.1 ns. Please note that our work focuses on the optical channel, so our setups and results are independent of the characteristics of transceiver front-ends.

V. CHANNEL CHARACTERIZATION

A. Overall Statistics

1) *Channel Gain*: Fig. 5 shows a glimpse of one complete record on channel gain along with the complete trajectory shown in Fig. 4(a). Note that in order to show the whole case, including sitting motions, we did not delete the records on the sojourn. However, for sake of mobility analysis, we rescaled the records during sojourn states, shrinking the period of the sojourn in a resident spot to 1000 times shorter in Fig. 5. Furthermore, in the following statistics, due to the same reason, we exclude the records on stationary status and focus on moving periods exclusively. In Fig. 5, one may find the relevance between different BSs owing to the geometric symmetry of the room layout. Sometimes this relevance shows up as similarity on channel gains such as in BS 1 and BS 3. However, sometimes it emerges as a kind of complementarity if one had noticed BS 1 and BS 2 for instance. Basically, the channel gain in uplink is close to that in downlink; however, the uplink holds an obviously higher probability of outage. In this work, LOS outages are defined as complete occlusions in LOS rays, while NLOS outages are referred to complete occlusions in both LOS and NLOS rays. Such occlusions can be induced by being either blocked by any opaque objects or out of the FOV of the receiver.

Next, we examine the overall statistics of the channel gain. From Fig. 6(a), it is shown that the PDFs have multiple peaks for LOS links. When the MT is moving, it experiences different relative positions against the BSs in terms of orientation and distance, and thus the distribution of the channel gain is associated with the mobility pattern. As aforementioned, the users pass by some specific areas with higher probabilities; therefore, several peaks emerge in the PDF of the channel gain, which features the regularity of the channel status at those frequently visited spots. For the PDFs shown in Fig. 6(a), the channel gain \hat{H}_0 distribution is fitted by N_{LOS} parts of

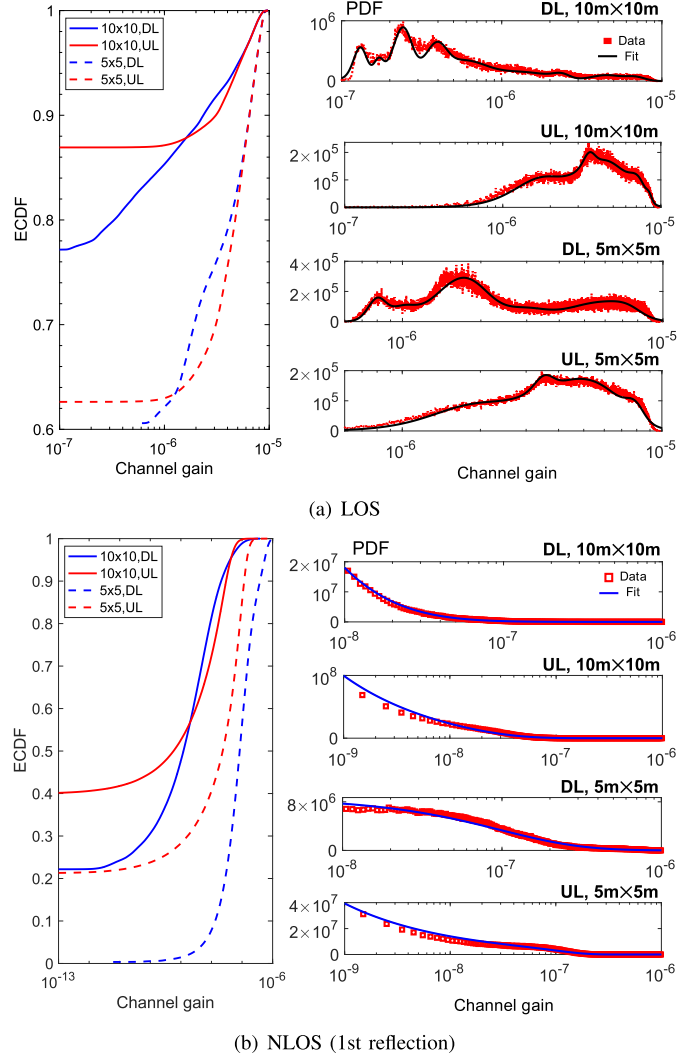


Fig. 6. Distributions of channel gain through all light links. The empirical cumulative distribution functions (ECDFs) illustrates overall statistics including outages, whereas the PDFs indicates the statistics and corresponding distribution fitting without outages. In (a), the multiple-peak Nakagami distributions are shown in the LOS PDFs for all LOS links. In (b), the channel gain statistics of the 1st reflection representing the major component in NLOS are shown, where their uplink distributions without outages subject to Gamma and Nakagami distribution, but for downlinks, Burr distributions.

Nakagami distribution with respective weights. The overall PDF of multiple-peak Nakagami distribution in LOS links is given as $f(\hat{H}_0) = f_{\text{MN}}(\hat{H}_0; k_n, \mu_n, \omega_n)$ where

$$f_{\text{MN}}(\hat{H}_0; k_n, \mu_n, \omega_n) = \sum_{n=1}^{N_{\text{LOS}}} k_n \frac{2\mu_n^{\mu_n} \hat{H}_0^{2\mu_n-1}}{\Gamma(\mu_n) \omega_n^{\mu_n}} e^{-\frac{\mu_n}{\omega_n} \hat{H}_0^2}, \quad (13)$$

in which $\Gamma(\mu_n)$ stands for the Gamma function, k_n represents the weights ($\sum k_n = 1$), μ_n stands for the shape parameter, and ω_n denotes the scale parameter. The detailed parameters of LOS channel gain distribution are listed in Table II.

On the other hand, for the 1st reflection representing the NLOS component shown in Fig. 6(b), the channel gain \hat{H}_1 without outages, however, adheres to conventional distributions. For the downlinks, the generalized log-logistic distributions (Burr Type XII distribution [34]) can be

TABLE II

LOS CHANNEL GAIN DISTRIBUTION FIT PARAMETERS
(MINIMAL DATA UNIT: 10^{-10})

UL, $10m \times 10m \times 3m$			
n	k_n	μ_n	ω_n
1	0.09	2.79	3.14×10^8
2	0.75	1.93	2.47×10^9
3	0.03	40.43	1.25×10^9
4	0.015	1.82×10^2	7.13×10^9
5	0.115	21.28	5.31×10^9
UL, $5m \times 5m \times 3m$			
n	k_n	μ_n	ω_n
1	0.06	3.10	3.38×10^8
2	0.03	38.97	1.25×10^9
3	0.79	2.19	3.14×10^9
4	0.06	46.21	6.28×10^9
5	0.06	2.36	8.32×10^8
DL, $10m \times 10m \times 3m$			
n	k_n	μ_n	ω_n
1	1.60×10^{-2}	28.38	1.75×10^6
2	6.10×10^{-2}	15.03	5.99×10^6
3	6.10×10^{-2}	12.46	1.59×10^7
4	8.00×10^{-3}	53.29	2.92×10^6
5	3.00×10^{-1}	0.96	2.45×10^8
6	5.00×10^{-2}	18.59	5.72×10^8
7	2.00×10^{-1}	6.84	2.07×10^9
8	2.00×10^{-1}	10.44	4.65×10^9
9	1.10×10^{-1}	2.36	3.72×10^7
DL, $5m \times 5m \times 3m$			
n	k_n	μ_n	ω_n
1	2.00×10^{-2}	42.80	6.42×10^7
2	2.60×10^{-1}	5.60	3.16×10^8
3	7.00×10^{-2}	19.36	5.47×10^9
4	1.10×10^{-1}	5.80	8.61×10^8
5	2.20×10^{-2}	17.22	9.94×10^7
6	5.18×10^{-1}	3.49	3.84×10^9

applied as $f(\hat{H}_1) = f_B(\hat{H}_1; c_B, k_B, \lambda_B)$ where

$$f_B(\hat{H}_1; c_B, k_B, \lambda_B) = \frac{c_B k_B}{\lambda_B} \left(\frac{\hat{H}_1}{\lambda_B} \right)^{c_B-1} \left[1 + \left(\frac{\hat{H}_1}{\lambda_B} \right)^{c_B} \right]^{-k_B-1}, \quad (14)$$

in which c_B, k_B, λ_B correspond to the first and second shape parameters, and the scale parameter, respectively. However for the uplinks in 1st reflection NLOS links, the distributions for different scenarios diverged as \hat{H}_1 for the $10m \times 10m \times 3m$ layout subjects to Gamma distribution as

$$f_G(\hat{H}_1; a_G, b_G) = \frac{\hat{H}_1^{a_G-1} e^{-\frac{\hat{H}_1}{b_G}}}{b_G^{a_G} \Gamma(a_G)}, \quad (15)$$

where a_G and b_G denote the parameters of shape and scale, respectively; and for the NLOS uplinks in $5m \times 5m \times 3m$ layout, it subjects to Nakagami distribution as

$$f_N(\hat{H}_1; \mu, \omega) = \frac{2\mu^\mu \hat{H}_1^{2\mu-1}}{\Gamma(\mu)\omega^\mu} e^{(-\frac{\mu}{\omega}\hat{H}_1^2)}, \quad (16)$$

where the detailed parameters of NLOS channel gain distribution are listed in Table III.

2) *Bandwidth*: In view of the high probability of outages in LOS transmissions, the NLOS standalone channels should also be considered, thereby increasing the flexibility and stability of deploying Li-Fi in mobile scenarios. The connectivity of NLOS standalone links is much higher as shown in Fig. 6,

TABLE III

NLOS CHANNEL GAIN DISTRIBUTION FIT PARAMETERS
(MINIMAL DATA UNIT: 10^{-10})

UL, $10m \times 10m \times 3m$		
a_G	b_G	
4.99×10^{-1}	3.00×10^2	
UL, $5m \times 5m \times 3m$		
μ	ω	
2.77×10^{-1}	5.65×10^5	
DL, $10m \times 10m \times 3m$		
λ_B	c_B	k_B
1.13×10^3	5.83×10^{-1}	6.49
DL, $5m \times 5m \times 3m$		
λ_B	c_B	k_B
6.71×10^3	9.90×10^{-1}	5.53

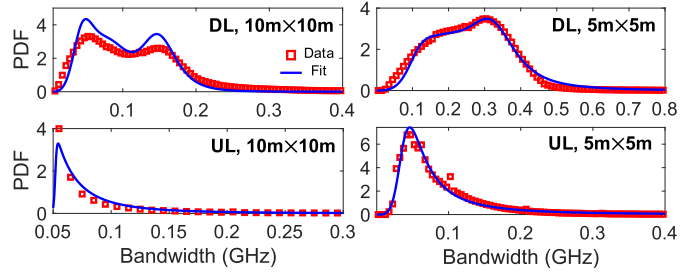


Fig. 7. PDF of -3 dB modulation bandwidth (BW) through all optical NLOS standalone links, where the fitting curves are also shown. The uplink bandwidth follows generalized log-logistic distributions and the downlink bandwidth follows multiple-peak log-logistic distributions.

and NLOS links could maintain communications to a certain extent when LOS links are blocked. However, due to multipath effect in NLOS links, the modulation bandwidth is limited, and therefore deserves a special investigation. As illustrated in Fig. 7, we fit the PDF of the uplink bandwidth \hat{B} using the generalized log-logistic distribution as $f(\hat{B}) = f_B(\hat{B}; c_B, k_B, \lambda_B)$

$$f_B(\hat{B}; c_B, k_B, \lambda_B) = \frac{c_B k_B}{\lambda_B} \left(\frac{\hat{B}}{\lambda_B} \right)^{c_B-1} \left[1 + \left(\frac{\hat{B}}{\lambda_B} \right)^{c_B} \right]^{-k_B-1}. \quad (17)$$

However, for downlinks, the bandwidth follows multiple-peak log-logistic distributions as $f(\hat{B}) = f_{ML}(\hat{B}; k_n, \mu_n, \sigma_n)$, where

$$f_{ML}(\hat{B}; k_n, \mu_n, \sigma_n) = \sum_{n=1}^{N_{BW}} k_n \frac{e^{z_n}}{\sigma_n \hat{B} (1 + e^{z_n})^2}, \quad (18)$$

in which $z_n = \frac{\log(\hat{B}) - \mu_n}{\sigma_n}$ and μ_n and σ_n correspond to the mean of logarithmic values and the scale parameter of logarithmic values, respectively, for the n -th peak. The detailed parameters of NLOS bandwidth distribution are listed in Table IV.

3) *Statistical Divergence*: Such divergence both between LOS and NLOS and in different room layouts implies a close entanglement of the channel statistics with environment-confined mobility details spatially and temporally. The multi-peak probability distribution in LOS channel gain clearly expresses the influence of the trajectory-environment interaction pattern on the channel gain distribution.

TABLE IV
BANDWIDTH DISTRIBUTION FIT PARAMETERS
(MINIMAL DATA UNIT: 0.1Hz)

UL, 10m×10m×3m			
λ_B	c_B	k_B	
5.19×10^8			
	7.02×10^1	2.92×10^{-2}	
UL, 5m×5m×3m			
λ_B	c_B	k_B	
8.28×10^8			
	5.34	2.62×10^{-1}	
DL, 10m×10m×3m			
n	k_n	μ_n	σ_n
1	0.3	20.7	2.08×10^{-1}
2	0.35	21.8	9.92×10^{-2}
3	0.35	21.3	2.03×10^{-1}
DL, 5m×5m×3m			
n	k_n	μ_n	σ_n
1	0.1	21.0	1.89×10^{-1}
2	0.3	21.9	1.13×10^{-1}
3	0.6	21.6	2.75×10^{-1}

However, such interaction pattern is not noticeable through NLOS statistics of channel gain or bandwidth. Thus, we can no longer use a single statistical model to summarize the indoor optical channel. It also inspires us to explore further the temporal and spatial characteristics behind these distributions.

4) Comparison With Random Waypoint-Based Model:

As a conventional random waypoint-based channel statistic proposed in [14], it gives that the channel gain follows Rayleigh distribution. However, our statistics show that the outage probability is higher during terminal movement, and the pattern of channel gain distribution highly depends on the environment-confined mobility pattern, which cannot be modeled using a simple stochastic model. The most recent statistic in [15], [23]–[25], [33] considering random terminal orientation suggests that for stationary users, the channel gain follows the modified truncated Laplace model and the modified Beta model, and for mobile users, it follows the sum of modified truncated Gaussian model and the sum of modified Beta model. However, since the user mobility in [15], [23]–[25], [33] is assumed as the random waypoint model, likewise, its user trajectory distribution cannot reflect the influences from the frequency and periodic pattern of visiting each location according to the macro mobility pattern, i.e., when to go and where to go. Different spatio-temporal trajectory proportions yield different channel statistics, and this is why our proposed statistics differ from the random waypoint-based ones after taking into account the nature of human behavior. More importantly, we can elaborate deeply on more details featuring the spatio-temporal evolution in channel statistics.

B. Spatial Features

Next, we investigate the spatial characteristics of the outage probability. The spatial distributions of LOS outage probability in $10m \times 10m$ and $5m \times 5m$ room layouts are illustrated in Fig. 8(a), (b), (c), and (d). The results for both uplink and downlink confirm the higher probability of outage at the intersections around the entrance as well as the resident nodes apart from the central area. This is due to the fact that the steering motion of user prompts turbulence in orientation. Because of the asymmetry in coverage, the distribution patterns in both

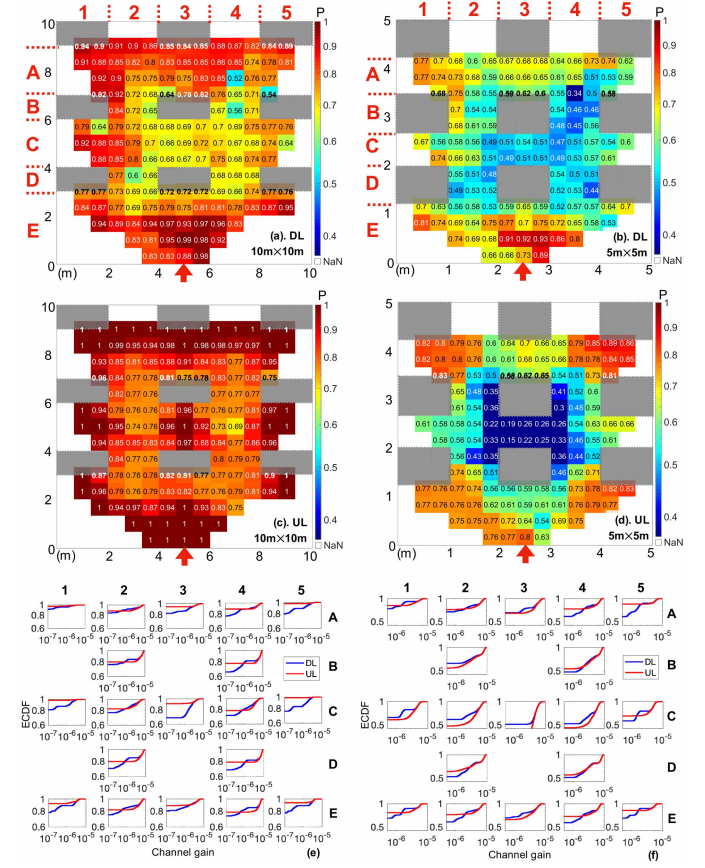


Fig. 8. Spatial outage probabilities and ECDFs of LOS channel gain. ECDFs are carried out outside furnishings area indexed through A to E vertically and through 1 to 5 horizontally. The black blocks ■ denote the furnishings areas and the red arrows ↑ stand for the entrances.

directions are not identical as the uplinks show a steeper gradient in spatially outage probability changes.

Then, we examine the spatial features in ECDFs of LOS channel gain, as depicted in Fig. 8(e) and (f). Although the ECDFs in different regions present apparent differences, they generally exhibit geometric symmetry. This geometrical feature is inherited from the symmetry of the furnishings and BS layout. These results illustrate a better channel state in the middle, but more severe features at the edges. The areas with better channel conditions contain the most aisles. In particular, the sub-figures in the middle parallel to the horizontal direction (Row C: $y \in (4m, 6m)$ in $10m \times 10m$ and $y \in (2m, 2.75m)$ in $5m \times 5m$) represent the area where users tend to pass by with a higher probability. Nevertheless, the uplink still outperforms the downlink slightly with a higher mean channel gain once there exists a received signal (also can be noticed from Fig. 6), and this fact is due to the difference in incident angle between transmitters and receivers.

However, the spatial patterns in NLOS links as shown in Fig. 9 exhibit different behavior. For uplinks, we find more outages around the entrance area, but we notice there are fewer outages around the entrance in downlink. The remaining areas demonstrate a stationary spatial pattern since the blockages and FOV cannot totally conceal all the diffused rays. This also limits the spatial variation range in bandwidth statistics since the key point to limiting bandwidth is the received ray

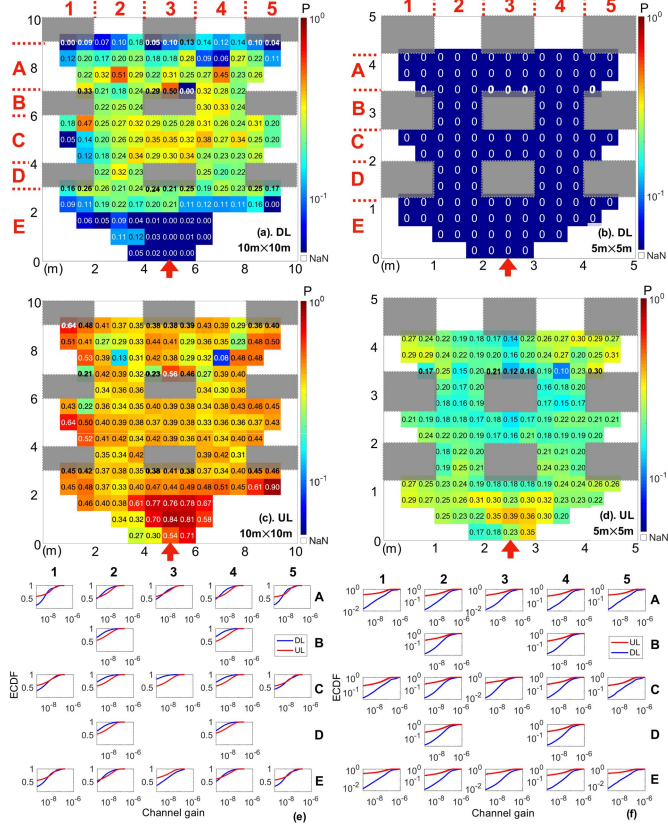


Fig. 9. Spatial outage probabilities and ECDFs of NLOS channel gain. ECDFs are carried out outside furnishings area indexed through **A** to **E** vertically and through **1** to **5** horizontally. The black blocks ■ denote the furnishings areas and the red arrows ↑ stand for the entrances.

delay spread, where the arrival time of a ray depends on the light path length rather than the relative angle between the transceivers.

It should be highlighted that the spatial statistics are not sufficient to understand the performance of indoor optical mobile channel. We ought to introduce the temporal statistics that are collected within a specific time window, during which the user trajectory follows the distribution illustrated in Fig. 4(b) and (d) with respect to the time interval. When evaluating the overall performance, the spatial features alone are not enough since the frequency of visiting a specific area is not taken into account. However, in the temporal statistics, the average outage probability during a certain time interval is a combination of all possible spatial distributions with the corresponding weights (frequency of visits). Thus, the temporal and spatial behaviors seem different. That is why we also need to study the temporal characteristics to reveal deeper aspects in the next subsection.

C. Temporal Features

Fig. 10 presents the complete temporal structure of the mobility pattern, where time indices of different traces are unified and categorized into 1000 intervals, and then channel statistics are conducted, respectively. The temporal pattern and its dependence on trajectories are illustrated by an explicit exposure on the channel statistics evolution throughout the motion of entering, wandering and exiting.

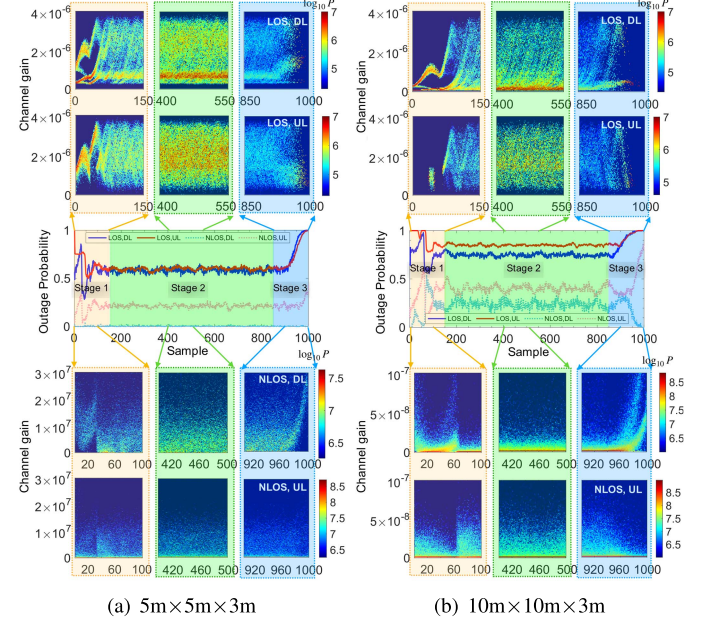


Fig. 10. Temporal outage probability and PDF of channel gain with respect to time along the course of entire trajectories. Time indices of different traces are unified and then classified into 1000 intervals in which outage statistics are carried out respectively. Stages 1 to 3 correspond to the three time-blocks during the entering, wandering and exiting movements.

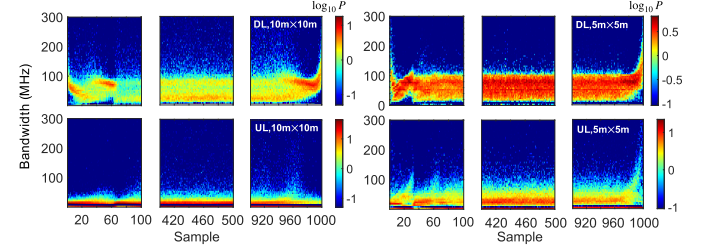


Fig. 11. PDFs of -3 dB modulation bandwidth with respect to time along the course of 3 stages.

Additionally, Fig. 11 illustrates the impact of mobility on bandwidth in NLOS links. We discuss the results according to the following stages:

1) Stage 1 (Entering): For the LOS component, the temporal evolution of the extreme channel states while moving from the entrance to the first destination is revealed at Stage 1 (entering stage). For the uplink in both room layouts, the outage probabilities begin with 100%, then fall sharply in a volatile manner, then slightly rise up, and afterward wanders around 60% in the $5m \times 5m$ room layout and 85% in the $10m \times 10m$ room layout. However, for the downlink, the outage probability in the $5m \times 5m$ layout begins with around 50% and then fluctuates in a broad range of 50% until it wanders around 60%, which is slightly lower than in the uplink. Whereas in the $10m \times 10m$ layout, the outage probability starts around 75%, then it also fluctuates in a broad range of 40% until wandering around 70%. As for the NLOS, the outage probability is much lower for the 1st reflection component than the LOS. In the $5m \times 5m$ room layout, the outage probability can hold below 1% in the downlink, and exhibits a similar behavior in the uplink as the LOS downlink but with outage probability around 20%. In the

$10m \times 10m$ layout, the outage probability of NLOS goes higher with broader dynamic range than that of LOS. As shown in Fig. 10, the PDFs of channel gain with respect to time along the course of Stage 1 is equivalent to an expansion of Fig. 6 in a successive temporal order. The influence of entering motion is very obvious. The peaks of the channel gain PDFs for the LOS component are shifting over time with the entering movement; whereas in NLOS links, although there is no prominent distribution peak, the shape of the PDF also changes with the entering movement. In this stage, as depicted in Fig. 11, the bandwidth distributions are not stable either, where the peaks vibrate while the PDF curves gradually broadens until the user reaches the first destinations.

We would like to highlight the view asymmetry between UL and DL. According to the statistics in Section IV.A, on average, the MT points to 31.79 degrees oblique upward, towards the position of BS when entering the room. However, during the first few steps after entering the $10m \times 10m$ room, the MT is outside the FOV of all BSs, causing the the UL outage probabilities in stage 1 begin at nearly 100%. As a matter of fact, each BS is stationary and fixed, pointing down to the ground, its receivable area limiting the UL reception is bounded by its FOV. On the other hand, the MT orients at the area of one of the BSs sometimes according to the user's random gesture, so the DL from such BS could probably fall inside the FOV of the MT. Therefore the MT has a higher probability to receive the DL signal in the $10m \times 10m$ room. Consequently, we get the result in Fig. 10(a), where the outage probabilities in stage 1 begin at 100% and 50% for UL and DL, respectively.

2) *Stage 2 (Wandering)*: After 100 intervals from the beginning of the trajectory, the outage probabilities become stationary random processes as denoted by Stage 2 (wandering stage). When the user is wandering within the room and shuttling among the resident nodes, the movement period is defined as wandering stage. The outage probability curves for uplink and downlink undergo consistent oscillations in Stage 2. Besides, the average outage probability in terms of time shown in Fig. 10 is higher than the outage probabilities presented from the spatial perspective of many areas as demonstrated in Fig. 8 since the areas with a high probability of outage are spatially small, but they are frequently passed by from the perspective of time. Meanwhile, the distribution characteristics are relatively stable. That is to say, from a time perspective, in addition to Stage 1 and Stage 3 (as will be interpreted later), the channel gain sequence can be seen as a stationary stochastic process with a multi-peak hybrid distribution. However, from a spatial perspective, given the differences among the statistics in each room layout, the distribution characteristics of the channel gain are still dominated by the spatial structure of the room layout. As for the bandwidth in Fig. 11, the PDF curves are becoming more stable as the user shuttles between different resident nodes.

3) *Stage 3 (Exiting)*: The last stage is defined as the motion of heading towards the exit (entrance) driven by the return tendency in the macro mobility. Generally, the channel dynamics in Stage 3 exhibit a distinct temporal symmetry toward the entering stage. The outage probabilities soar towards 100%

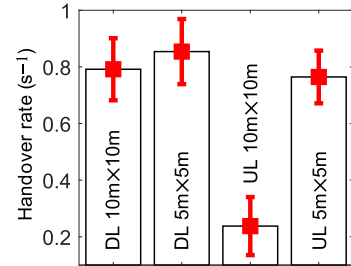


Fig. 12. Handover rate under out proposed indoor mobility.

before leaving the room except for the NLOS downlinks. In the PDFs of LOS channel gain, we find the peaks reciprocating among the distribution region over time; but the peaks of the PDFs of NLOS channel gain seem to shift to higher gain over time in this stage. The distribution peak diversion towards higher values emerging at the end of Stage 3 is also found in the PDFs of bandwidth apart from the uplink in $10m \times 10m$ room layout. Such peak diversions in the NLOS downlinks reflect the improvement in channel status with the outage rate's diminishing and the distribution peaks' rising in channel gain and bandwidth. Yet in other links, the channels are deteriorating along with the exiting movement due to the increase in outage occasions.

Changing the values of $t_{s,\min}$ and $t_{s,\max}$ only changes the starting time of existing stage, which affects the duration of the wandering stage, since the user only comes into the room and exits the room once. For the statistics in the wandering stage, the channel gain distribution, bandwidth distribution, and outages probability can be seen as stationary stochastic processes, and therefore the duration of this stage does not have much impact on the reported results.

D. Handover Rate

Handovers are triggered among BSs to ascertain reliable connection with quality-of-service (QoS) guarantee. We assume the handover process overhead as 300 ms that is an average duration adopted in lecture [2], [35]–[39], and the BS with the best LOS channel gain will be designated as the target BS. During handover processes, the MTs dwell in the currently serving BS. The handover rate under the indoor mobility model is shown in Fig. 12. The means of handover rate are 0.79, 0.85, 0.24, 0.76 for the downlinks in $10m \times 10m$ room layout and $5m \times 5m$ room layout, and the uplinks in $10m \times 10m$ room layout and $5m \times 5m$ room layout, respectively. We note that the handover rate of uplink in the $10m \times 10m$ layout is actually not proportional to the outage risk. The reason of this fact is that the data stream has nowhere to be offloaded since all BSs are suffering poor links under such high outage risks, which in turn undermines the handover rate. Of course, this ill-conditioned result is caused by poor link management. Therefore, in view of human indoor mobility characteristics, a more intelligent methodology on network resource management is what this field desperately needs.

Under our proposed mobility model, the handover rate is higher than that in [39], since the entering and existing movements raise the outage probability, which in turn results

in higher handover rate. Such entering and existing stages were not considered in [39].

VI. CONCLUSION

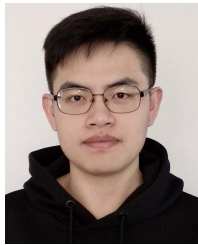
In this work, we have first proposed an approach to produce indoor human mobility so as to tackle the shortage and difficulty in collecting indoor mobility data sets. In the proposed mobility model, the macro pattern is featured by a semi-Markov renewal process subject to bounded Lévy-walk and return regularity, and the micro pattern is featured by the shortest path, steering behavior, and random terminal orientation. Parameters of this model are obtained by fitting the mobility model with measurement results collected from the real-world. Thus, we have generated sequences of the CIR over the entire trajectories, in which judgment on blockages from furnishings and user body is applied upon every single ray in advance.

From our dataset of channel information, the spatio-temporal channel characterization of mobile OWC has been unveiled. As for the LOS links, the overall channel gain follows multiple-peak Nakagami distributions. As for the NLOS links, the channel gain distributions in uplinks without outages subject to Gamma and Nakagami distribution, but for downlinks, they follow Burr distributions. The uplink bandwidth in NLOS follows the generalized log-logistic distribution; while for downlinks, the NLOS bandwidth follows multiple-peak log-logistic distributions. All these distributions are space-time-dependent. The outage probability exhibits an apparent spatial symmetry. From the perspective of time, the probability distributions of outage and channel gain are basically stationary while user's wandering indoor, and are dominated by the trajectories. However, along the way towards the first entrance or exit point driven by the macro mobility patterns, these distributions suffer from a strong disturbance with evolution over time; whereas from a spatial perspective, the distributions of the channel gain are still dominated by spatial structures. The conventional handover rate analysis under the proposed environment-confined mobility yields ill-conditioned results owing to frequent outages, which motivates further investigations on more intelligent methodology on mobile OWC network planning and resource management strategies.

REFERENCES

- [1] A. Jovicic, J. Li, and T. Richardson, "Visible light communication: Opportunities, challenges and the path to market," *IEEE Commun. Mag.*, vol. 51, no. 12, pp. 26–32, Dec. 2013.
- [2] H. Haas, L. Yin, Y. Wang, and C. Chen, "What is LiFi?" *J. Lightw. Technol.*, vol. 34, no. 6, pp. 1533–1544, Mar. 15, 2016.
- [3] H. Haas, C. Chen, and D. O'Brien, "A guide to wireless networking by light," *Prog. Quantum Electron.*, vol. 55, pp. 88–111, Sep. 2017.
- [4] J. Armstrong, Y. Sekercioglu, and A. Neild, "Visible light positioning: A roadmap for international standardization," *IEEE Commun. Mag.*, vol. 51, no. 12, pp. 68–73, Dec. 2013.
- [5] I. Moreno and C.-C. Sun, "Modeling the radiation pattern of LEDs," *Opt. Express*, vol. 16, no. 3, pp. 1808–1819, Feb. 2008.
- [6] J. Ding, Z. Xu, and L. Hanzo, "Accuracy of the point-source model of a multi-LED array in high-speed visible light communication channel characterization," *IEEE Photon. J.*, vol. 7, no. 4, pp. 1–14, Aug. 2015.
- [7] J. M. Kahn and J. R. Barry, "Wireless infrared communications," *Proc. IEEE*, vol. 85, no. 2, pp. 265–298, Feb. 1997.
- [8] H. Schulze, "Frequency-domain simulation of the indoor wireless optical communication channel," *IEEE Trans. Commun.*, vol. 64, no. 6, pp. 2551–2562, Jun. 2016.
- [9] K. Lee, H. Park, and J. R. Barry, "Indoor channel characteristics for visible light communications," *IEEE Commun. Lett.*, vol. 15, no. 2, pp. 217–219, Feb. 2011.
- [10] V. Jungnickel, V. Pohl, S. Nonnig, and C. von Helmolt, "A physical model of the wireless infrared communication channel," *IEEE J. Sel. Areas Commun.*, vol. 20, no. 3, pp. 631–640, Apr. 2002.
- [11] S. P. Rodríguez, R. P. Jiménez, B. R. Mendoza, F. J. L. Hernández, and A. J. A. Alfonso, "Simulation of impulse response for indoor visible light communications using 3D CAD models," *EURASIP J. Wireless Commun. Netw.*, vol. 2013, no. 1, p. 7, Dec. 2013.
- [12] C. Chen, D. A. Basnayaka, X. Wu, and H. Haas, "Efficient analytical calculation of non-line-of-sight channel impulse response in visible light communications," *J. Lightw. Technol.*, vol. 36, no. 9, pp. 1666–1682, May 1, 2018.
- [13] F. Miramirkhani, O. Narmanlioglu, M. Uysal, and E. Panayirci, "A mobile channel model for VLC and application to adaptive system design," *IEEE Commun. Lett.*, vol. 21, no. 5, pp. 1035–1038, May 2017.
- [14] P. Chvojka, S. Zvanovec, P. A. Haigh, and Z. Ghassemlooy, "Channel characteristics of visible light communications within dynamic indoor environment," *J. Lightw. Technol.*, vol. 33, no. 9, pp. 1719–1725, May 1, 2015.
- [15] M. D. Soltani, A. A. Purwita, Z. Zeng, H. Haas, and M. Safari, "Modeling the random orientation of mobile devices: Measurement, analysis and LiFi use case," *IEEE Trans. Commun.*, vol. 67, no. 3, pp. 2157–2172, Mar. 2019.
- [16] H. Marshoud, V. M. Kapinas, G. K. Karagiannidis, and S. Muhaidat, "Non-orthogonal multiple access for visible light communications," *IEEE Photon. Technol. Lett.*, vol. 28, no. 1, pp. 51–54, Jan. 1, 2016.
- [17] A. Sewaiwar, S. V. Tiwari, and Y. H. Chung, "Mobility support for full-duplex multiuser bidirectional VLC networks," *IEEE Photon. J.*, vol. 7, no. 6, pp. 1–9, Dec. 2015.
- [18] L. Yin and H. Haas, "Physical-layer security in multiuser visible light communication networks," *IEEE J. Sel. Areas Commun.*, vol. 36, no. 1, pp. 162–174, Jan. 2018.
- [19] I. Rhee, M. Shin, S. Hong, K. Lee, S. J. Kim, and S. Chong, "On the levy-walk nature of human mobility," *IEEE/ACM Trans. Netw.*, vol. 19, no. 3, pp. 630–643, Jun. 2011.
- [20] M. C. Gonzalez, C. A. Hidalgo, and A.-L. Barabasi, "Understanding individual human mobility patterns," *Nature*, vol. 453, no. 7196, p. 779, 2008.
- [21] E. W. Dijkstra, "A note on two problems in connexion with graphs," *Numerische Math.*, vol. 1, no. 1, pp. 269–271, Dec. 1959.
- [22] C. W. Reynolds, "Steering behaviors for autonomous characters," in *Proc. Game Developers Conf.*, vol. 1999, 1999, pp. 763–782.
- [23] I. Tavakkolnia *et al.*, "MIMO system with multi-directional receiver in optical wireless communications," in *Proc. IEEE Int. Conf. Commun. Workshops (ICC Workshops)*, May 2019, pp. 1–6.
- [24] M. D. Soltani *et al.*, "Bidirectional optical spatial modulation for mobile users: Toward a practical design for LiFi systems," *IEEE J. Sel. Areas Commun.*, vol. 37, no. 9, pp. 2069–2086, Sep. 2019.
- [25] M. A. Arfaoui *et al.*, "SNR statistics of indoor mobile VLC users with random device orientation," in *Proc. IEEE Int. Conf. Commun. Workshops (ICC Workshops)*, May 2019, pp. 1–6.
- [26] H. Farooq and A. Imran, "Spatiotemporal mobility prediction in proactive self-organizing cellular networks," *IEEE Commun. Lett.*, vol. 21, no. 2, pp. 370–373, Feb. 2017.
- [27] A. Nadembega, A. Hafid, and T. Taleb, "A destination and mobility path prediction scheme for mobile networks," *IEEE Trans. Veh. Technol.*, vol. 64, no. 6, pp. 2577–2590, Jun. 2015.
- [28] A. A. Purwita, M. D. Soltani, M. Safari, and H. Haas, "Terminal orientation in OFDM-based LiFi systems," *IEEE Trans. Wireless Commun.*, vol. 18, no. 8, pp. 4003–4016, Aug. 2019.
- [29] J. R. Barry, J. M. Kahn, W. J. Krause, E. A. Lee, and D. G. Messerschmitt, "Simulation of multipath impulse response for indoor wireless optical channels," *IEEE J. Sel. Areas Commun.*, vol. 11, no. 3, pp. 367–379, Apr. 1993.
- [30] L. Zeng *et al.*, "High data rate multiple input multiple output (MIMO) optical wireless communications using white LED lighting," *IEEE J. Sel. Areas Commun.*, vol. 27, no. 9, pp. 1654–1662, Dec. 2009.
- [31] Advanced Tools for Smartphone-Based Experiments: Phyphox. Accessed: Oct. 2018. [Online]. Available: <https://phyphox.org/>

- [32] B. J. Mohler, W. B. Thompson, S. H. Creem-Regehr, H. L. Pick, and W. H. Warren, "Visual flow influences gait transition speed and preferred walking speed," *Exp. Brain Res.*, vol. 181, no. 2, pp. 221–228, Aug. 2007.
- [33] M. Amine Arfaoui *et al.*, "Measurements-based channel models for indoor LiFi systems," 2020, *arXiv:2001.09596*. [Online]. Available: <http://arxiv.org/abs/2001.09596>
- [34] I. W. Burr, "Cumulative frequency functions," *Ann. Math. Statist.*, vol. 13, no. 2, pp. 215–232, Jun. 1942.
- [35] Y. Wang, D. A. Basnayaka, X. Wu, and H. Haas, "Optimization of load balancing in hybrid LiFi/RF networks," *IEEE Trans. Commun.*, vol. 65, no. 4, pp. 1708–1720, Apr. 2017.
- [36] Z. Zeng, M. Dehghani Soltani, Y. Wang, X. Wu, and H. Haas, "Realistic indoor hybrid WiFi and OFDMA-based LiFi networks," *IEEE Trans. Commun.*, vol. 68, no. 5, pp. 2978–2991, May 2020.
- [37] M. A. Dastgheib, H. Beyranvand, J. A. Salehi, and M. Maier, "Mobility-aware resource allocation in VLC networks using T-step look-ahead policy," *J. Lightw. Technol.*, vol. 36, no. 23, pp. 5358–5370, Dec. 1, 2018.
- [38] Y. Wang and H. Haas, "Dynamic load balancing with handover in hybrid Li-Fi and Wi-Fi networks," *J. Lightw. Technol.*, vol. 33, no. 22, pp. 4671–4682, Nov. 15, 2015.
- [39] X. Wu and H. Haas, "Handover skipping for LiFi," *IEEE Access*, vol. 7, pp. 38369–38378, 2019.



Zi-Yang Wu received the B.S. degree in electronic science and technology and the M.S. degree in circuits and systems from Northeastern University, Shenyang, China, in 2014 and 2016, respectively, where he is currently pursuing the Ph.D. degree in electrical and electronic engineering. He was also a joint Ph.D. Student with the Department of Electrical and Computer Engineering, Texas A&M University, College Station, USA, from 2018 to 2019. His research interests include wireless communications and machine learning.



Muhammad Ismail (Senior Member, IEEE) received the B.Sc. (Hons.) and M.Sc. degrees in electrical engineering (electronics and communications) from Ain Shams University, Cairo, Egypt, in 2007 and 2009, respectively, and the Ph.D. degree in electrical and computer engineering from the University of Waterloo, Waterloo, ON, Canada, in 2013. He is currently an Assistant Professor with the Department of Computer Science, Tennessee Tech University, Cookeville, TN, USA. He was a co-recipient of the Best Paper Awards at IEEE ICC 2014, IEEE Globecom 2014, SGRE 2015, and Green 2016 and the Best Conference Paper Award from the IEEE Communications Society Technical Committee on Green Communications and Networking at IEEE ICC 2019. He was the Workshop Co-Chair for IEEE Greencom 2018, the TPC Co-Chair for IEEE VTC 2017 and 2016, the Publicity and Publication Co-Chair for CROWNCOM 2015, and the Web-Chair for IEEE INFOCOM 2014. He is an Associate Editor of IEEE IoT JOURNAL, IEEE TRANSACTIONS ON GREEN COMMUNICATIONS AND NETWORKING, IET Communications, and PHYCOM (Elsevier). He was an Editorial Assistant of IEEE TRANSACTIONS ON VEHICULAR TECHNOLOGY from 2011 to 2013. He has been a Technical Reviewer for several IEEE conferences and journals.



Justin Kong (Member, IEEE) received the B.S. and Ph.D. degrees in electrical engineering from Korea University, Seoul, South Korea, in 2009 and 2015, respectively. In 2010, he visited the University of Southern California, Los Angeles, CA, USA, to conduct collaborative research. In 2015, he was a Post-Doctoral Research Professor with Korea University. From 2015 to 2018, he was a Post-Doctoral Research Fellow with Nanyang Technological University, Singapore. He was a Post-Doctoral Research Associate with Texas A&M University from 2018 to 2019. In 2019, he joined the U.S. Army Research Laboratory, where he is currently a Post-Doctoral Fellow. His research interests include information theory, signal processing for wireless communications, and stochastic geometry and its applications in wireless communications. He received the Bronze Prize at the Samsung Humantech Paper Contest in 2012 and 2013. He was a recipient of the IEEE TCGCN Best Paper Award at IEEE ICC 2019.



Erchin Serpedin (Fellow, IEEE) is currently a Professor with the Electrical and Computer Engineering Department, Texas A&M University, College Station. He has authored three research monographs, one textbook, 17 book chapters, 170 journal articles, and 270 conference papers. His current research interests include signal processing, machine learning, artificial intelligence, cybersecurity, smart grids, and wireless communications. He served as an Associate Editor for more than 12 journals, including journals such as IEEE TRANSACTIONS ON INFORMATION THEORY, IEEE TRANSACTIONS ON SIGNAL PROCESSING, IEEE TRANSACTIONS ON COMMUNICATIONS, IEEE SIGNAL PROCESSING LETTERS, IEEE COMMUNICATIONS LETTERS, IEEE TRANSACTIONS ON WIRELESS COMMUNICATIONS, IEEE Signal Processing Magazine, and Signal Processing (Elsevier) and as the Technical Chair for six major conferences.



Jiao Wang received the Ph.D. degree in pattern recognition and intelligent system from Northeastern University, Shenyang, China, in 2006. He was a Research Fellow at Microsoft Asia in 2007. He is currently a Professor with the College of Information Science and Engineering, Northeastern University. He is the Director of the Institute of Advanced Learning and Advanced Intelligent Decision Making, Northeastern University, and the Director of the Machine Game Committee of the China Association of Artificial Intelligence (CAAI). His research interests include machine learning and computer games theory.